Journal of Power Sources 201 (2012) 95–102

Contents lists available at SciVerse ScienceDirect

Journal of Power Sources

journal homepage: www.elsevier.com/locate/jpowsour

# Electrochemical characteristics of $La_{0.8}Sr_{0.2}Cr_{0.82}Ru_{0.18}O_{3-\delta}$–$Gd_{0.1}Ce_{0.9}O_2$ solid oxide fuel cell anodes in $H_2$–$H_2O$–CO–$CO_2$ fuel mixtures

D.M. Bierschenk, S.A. Barnett*

*Department of Materials Science and Engineering, Northwestern University, Evanston, IL 60208, USA*

ARTICLE INFO

*Article history:*
Received 24 August 2011
Received in revised form 29 October 2011
Accepted 31 October 2011
Available online 6 November 2011

*Keywords:*
Anode
Electrochemical impedance spectroscopy
Coal gas
Solid oxide fuel cell
Oxide
Carbon monoxide

ABSTRACT

This paper describes the performance of composite $La_{0.8}Sr_{0.2}Cr_{0.82}Ru_{0.18}O_{3-\delta}$–$Gd_{0.1}Ce_{0.9}O_2$ anodes operated in varied $H_2O$–$H_2$, CO–$CO_2$, and $H_2O$–$H_2$–CO–$CO_2$ fuel mixtures. Impedance spectroscopy studies in both $H_2O$–$H_2$ and CO–$CO_2$ showed two main impedance responses that were thermally activated and exhibited power law variation with gas partial pressures. The polarization resistances in CO–$CO_2$ mixtures were larger than in $H_2$–$H_2O$ mixtures with the same partial pressure ratios. Polarization resistances for surrogate coal syngas $H_2O$–$H_2$–CO–$CO_2$ fuel mixtures were higher than for $H_2O$–$H_2$–Ar mixtures with the same $H_2$ and $H_2O$ partial pressures, indicating that CO or $CO_2$ interfered with the $H_2$ oxidation reaction.


## 1. Introduction

Solid oxide fuel cell (SOFC) systems are typically designed to utilize practical fuels such as reformed hydrocarbons or gasified coal, such that the anodes ultimately operate in mixtures of CO, $CO_2$, $H_2$, $H_2O$, and in some cases $CH_4$. While the electrochemical characteristics of Ni-based anodes in $H_2$–$H_2O$ fuels have been studied in considerable detail, and there are a number of reports on hydrocarbon operation [1,2], there have been relatively few reports on CO–$CO_2$ fuel mixtures [3–5]. Based on results that show much higher polarization resistance in CO–$CO_2$ than for $H_2$–$H_2O$ [5], it is often assumed that the $H_2$ oxidation reaction entirely dominates the anode characteristics, although this view is challenged by very recent work [3]. Even if CO and $CO_2$ are essentially inert, CO oxidation can still occur indirectly via the water-gas shift reaction in anodes such as Ni–8 mol% $Y_2O_3$-stabilized $ZrO_2$ (YSZ) that have catalytic activity [7]. Relatively little information is available on the characteristics of alternative oxide anode materials in CO- and $CO_2$-containing fuels [6,8].

The present contribution describes an electrochemical impedance spectroscopy (EIS) study of a composite anode consisting of $La_{0.8}Sr_{0.2}Cr_{0.82}Ru_{0.18}O_{3-\delta}$ (LSCrRu) and $Gd_{0.1}Ce_{0.9}O_2$ (GDC). This anode material was chosen as an example of a conducting-oxide anode material where a nano-scale catalyst material is employed to improve fuel oxidation kinetics [8–13]. Such anodes, along with conducting oxide materials without catalysts [14–17], have been studied by a number of researchers with the aim of improving upon Ni-YSZ with regard to susceptibility to coking, poisoning by fuel impurities such as $H_2S$ [18–23], degradation upon redox cycling [24,25], and the above-mentioned slow kinetics for CO oxidation. Preliminary results on the operation of SOFCs with LSCrRu–GDC anodes in coal gas were recently reported, including results showing that the anode was more stable in CO-rich fuels than Ni-YSZ [26]. In the present work, EIS was used to measure anode polarization resistance while systematically varying the temperature and partial pressures in CO–$CO_2$ and $H_2$–$H_2O$ fuel mixtures. These results were used in order to better understand electrochemical reaction kinetics in coal gas $H_2$–$H_2O$–CO–$CO_2$ mixtures. The results are compared with the literature data for Ni-YSZ.

## 2. Experimental procedures

### 2.1. Cell fabrication

The LSCrRu–GDC anodes were studied in $La_{0.9}Sr_{0.1}Ga_{0.8}Mg_{0.2}O_{3-\delta}$ (LSGM) [27] electrolyte-supported solid oxide fuel cells. The synthesis of LSCrRu and fabrication of cells have been described in detail previously [9], and are summarized here.

LSCrRu was prepared by solid-state reaction from oxides and carbonates. The precursors were wet ball milled in deionized water

* Corresponding author. Tel.: +1 847 491 2447; fax: +1 847 491 7820.
*E-mail address:* s-barnett@northwestern.edu (S.A. Barnett).

0378-7753/$ – see front matter © 2011 Elsevier B.V. All rights reserved.
doi:10.1016/j.jpowsour.2011.10.119

for 24 h, dried, and fired at 1200 °C for 3 h. The composite anode powder was prepared by mixing this powder with commercial GDC (Nex Tech) at a 1:1 weight ratio for 24 h via ball milling. The resulting powder was dried, ground, sieved (#120 mesh), and dispersed in a vehicle (V-737, Heraeus Inc., PA), using a three-roll mill to make an ink. A similar ink was prepared with the composition $La_{0.8}Sr_{0.2}CrO_3$ (LSCr) and was used as an anode current collector.

Cells were fabricated with $La_{0.6}Sr_{0.4}Fe_{0.8}Co_{0.2}O_{3-\delta}$ (LSCF, Praxair) – GDC composite cathodes and pure LSCF cathode current collectors. Cathode inks were also prepared by mixing LSCF and GDC (1:1 weight ratio) via wet ball milling. The resulting slurry was dried, sieved (#120 mesh), and suspended in Heraeus V-737 vehicle to form the cathode ink. The pure LSCF cathode current collector ink was prepared in a similar fashion.

The LSGM electrolyte material was prepared by solid-state reaction. Stoichiometric quantities of dried $La_2O_3$, $SrCO_3$, $Ga_2O_3$, and MgO were mixed and calcined at 1250 °C for 12 h. The resulting solid was ground, sieved, mixed with PVB and pressed into 19 mm diameter pellets weighing 0.45 g. The pellets were then sintered at 1450 °C for 6 h.

The LSCrRu–GDC and pure LSCr inks were applied to the LSGM supports by screen printing. The anode bi-layer was then fired at 1200 °C for 3 h. The cathode inks were then applied using screen printing. This cathode bi-layer was fired at 1000 °C for 3 h. Au current collector grids were applied to both electrodes by screen printing Au ink (Heraeus Inc., PA). The resulting fuel cells had a diameter of ~1.5 cm, an electrolyte thickness of ~0.3–0.4 mm, an anode thickness of ~15 μm and a cathode thickness of 20–30 μm. The anode and cathode areas were 0.5 $cm^2$. A few symmetrical cells with identical cathodes on both sides of the LSGM electrolyte were also prepared.

### 2.2. Cell testing

The cell testing configuration has been described in detail previously [28]. The cells were mounted for testing on alumina support tubes and sealed with Ag ink (DAD-87, Shanghai Research Institute of Synthetic Resins). Electrical contact to the cells was made with Ag wires. The fuel was supplied via a smaller diameter alumina tube placed inside the larger alumina support tube. Both alumina tubes were supported by a stainless steel manifold and sealed with viton o-rings to allow collection of the anode exhaust.

Testing of all cells was started in humidified hydrogen for ~100 h, the time typically required to reach steady state LSCrRu–GDC anode characteristics [9,10,13]. CO, Ar, $CO_2$, and $H_2$ (Airgas) flow rates were set with mass flow controllers (MKS). The steam partial pressure $p(H_2O)$ was controlled by flowing dry gas mixtures through a temperature controlled (Glas Col, 104A) humidifier containing deionized water. The $H_2O$ flow rate was determined from the bath temperature and the expected saturation vapor pressure of $H_2O$. The temperature variation of the humidifier was measured to be ±0.25 °C during experiments. This variation was found to result in fluctuations in the cell resistance of approximately ±0.3%. Condensation in fuel lines and exhaust during testing was avoided at high $p(H_2O)$ measurements by heating the gas lines above 100 °C.

The electrochemical impedance spectroscopy (EIS) measurements (IM6, Zahner) were done over a frequency range of 0.1 Hz to 1 MHz with a 20 mV ac potential amplitude at the open circuit voltage. Note that temperature-dependent measurements were normally done at ≥700 °C, since coking was expected at lower temperatures for the CO–$CO_2$-containing fuels. The cell impedance spectra were fit with Zview using either two or three Cole elements in series with a resistor and inductor.

Care was taken to quantify and, where possible, avoid sources of experimental error in impedance measurements. Variability in cell resistance during an ~24 h period was found to be <1% during measurements in 3% $H_2O$, 97%$H_2$,due in part to cell temperature fluctuations, but increased to 2% for 10% $H_2O$ in $H_2$, mainly due to the above-mentioned variability in bubbler temperature. In some cases, anode resistance could change by several percent over >12 h during equilibration after a change in test conditions. In order to avoid substantial errors from these transients without prohibitively long testing times, changes in cell conditions were normally done consistently (e.g., always decreasing a partial pressure) and EIS measurements were typically performed 0.5–1 h after the change. The mass flow controllers were calibrated before each experiment with a bubble meter, and flow rates did not appear to be a significant source of error. The maximum temperature error for the k-type thermocouples (Omega Engineering) was 0.75% of the temperature reading (°C); this fixed error had little effect on the activation energy values. Overall, the above polarization resistance error of ~2% resulted in activation energy errors of ±0.05 eV, and power law exponent errors of ±0.04.

**Table 1**
LSCF–GDC cathode symmetric cell data.

| Temperature (K) | $R_p$ (Ω $cm^2$) | Freq. (Hz) |
|---|---|---|
| 800 | 0.02 | 420 |
| 750 | 0.04 | 200 |
| 700 | 0.10 | 90 |

## 3. Results

The results of cell EIS measurements are described below for $H_2$–$H_2O$–Ar (Section 3.1), CO–$CO_2$–Ar (Section 3.2), and $H_2$–$H_2O$–CO–$CO_2$–$N_2$ fuel mixtures (Section 3.3). The results were acquired from a single cell in order to isolate the effects of different fuel compositions and temperatures. Results from several other cells verified that the results were representative. Scanning electron microscope images of these anodes showed a typical porous electrode microstructure, while transmission electron microscope images revealed the presence of Ru nano-particles on the chromite surfaces, similar to results presented in prior reports [9,10,13].

### 3.1. $H_2$–$H_2O$–Ar fuel

Fig. 1 shows Bode and Nyquist plots of EIS data taken at 800 °C at varied $H_2$ partial pressures, $p(H_2)$. The Ar/$H_2$ ratio was varied, but the total flow rate was maintained at 100 ml $min^{-1}$. The steam partial pressure $p(H_2O)$ was fixed at 0.1 atm by flowing the $H_2$–Ar mixtures through the fuel humidifier held at 47 °C. The Nyquist plot (Fig. 1b) showed that decreasing $p(H_2)$ from 0.9 to 0.3 atm resulted in a total polarization resistance $R_P$ increase from 0.28 to 0.37 Ω $cm^2$. The broad frequency range of the response in the Bode plot (Fig. 1a) and the depressed appearance of the arc in Fig. 1b suggested that more than one response was present, even though separate features were not resolved. EIS fitting was used to separate the components. A model with three Cole elements in series with an inductor and resistor was used. One Cole element was allocated to the cathode and its parameters were fixed by fitting EIS data from an LSCF/LSCF–GDC/LSGM/LSCF–GDC/LSCF cathode symmetric cell. The cathode resistance values are shown in Table 1. Good fits to the EIS data were obtained using two anode Cole elements, centered at ~100 Hz and ~1 Hz, and the fixed cathode Cole element, as shown in Fig. 1.

Fig. 2 shows the effect of $p(H_2O)$, varied by operating the humidifier at temperatures of 47, 61, 70, and 77 °C, on the EIS results at 800 °C. The total flow rate was maintained at 200 ml $min^{-1}$ and the Ar content was adjusted to maintain a constant $p(H_2)$. The results were similar to those shown in Fig. 1, with the total polarization

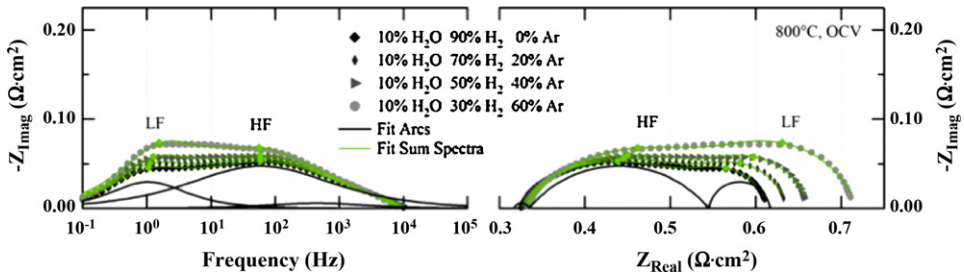


**Fig. 1.** Bode (left) and Nyquist (right) plots of the EIS data measured at 800 °C and open circuit with different $H_2$ partial pressures and fixed $H_2O$ partial pressure. The grey symbols indicate the measured data, green lines show the fits, black lines illustrate the individual fitted contributions for the high $p(H_2)$ case, and green symbols show the fitted elements' characteristic frequencies. (For interpretation of the references to color in this figure caption, the reader is referred to the web version of the article.)

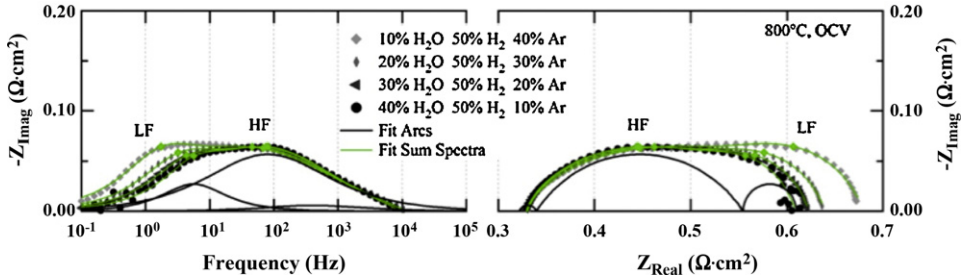


**Fig. 2.** Bode (left) and Nyquist (right) plots of the EIS data measured at 800 °C and open circuit with different $H_2O$ partial pressures and fixed $H_2$ partial pressure. The grey symbols indicate the measured data, green lines show the fits, black lines illustrate the individual fitted contributions for the high $p(H_2O)$ case, and green symbols show the fit characteristic frequencies. (For interpretation of the references to color in this figure caption, the reader is referred to the web version of the article.)

resistance generally increasing with decreasing $p(H_2O)$. Good fits to the EIS data were again obtained using the equivalent circuit with two anode Cole elements and a fixed cathode Cole element.

Fig. 3 shows log–log plots of the resistances $R_{HF}$ of the higher-frequency anode response and $R_{LF}$ of the lower-frequency anode response versus $p(H_2)$ (a) and $p(H_2O)$ (b). As shown in Fig. 3a, both responses followed a power law-type dependence, with $R_{HF} \propto p(H_2)^{-0.11}$ and $R_{LF} \propto p(H_2)^{-0.59}$. As shown in Fig. 3b, the dependence $R_{HF} \propto p(H_2O)^{-0.10}$ provided a good fit to the data, but the best fit $R_{LF} \propto p(H_2O)^{-0.37}$ to the low-frequency response was not very good. The dependence of these responses on fuel partial pressures indicates that they are related to anode processes.

The temperature dependent EIS response was measured between 700 and 800 °C in a fuel containing 25% $H_2O$ and 75% $H_2$. The data along with fits, using the same model as above, are shown in Fig. 4. Both $R_{HF}$ and $R_{LF}$ increased with decreasing temperature. The characteristic frequency of $R_{LF}$ remained almost constant at 3 Hz, while feature $R_1$ decreased from 97 Hz to 41 Hz. An Arrhenius plot of $R_{HF}$ and $R_{LF}$ in Fig. 5 shows that both processes are thermally activated with $E_{HF}$ = 1.1 eV and $E_{LF}$ = 0.66 eV. The cell ohmic resistance (not displayed) was also thermally activated with $E_{ohm}$ = 0.68 eV.

### 3.2. CO–$CO_2$–Ar fuel

The effect of the CO and $CO_2$ partial pressures on cell performance at 800 °C was also studied. The total fuel flow rate was maintained at 150 ml $min^{-1}$. Fig. 6 shows EIS data taken at varied CO partial pressures, $p(CO)$, and fixed $CO_2$ partial pressure, $p(CO_2)$ = 0.33 atm. The Nyquist plot (Fig. 6b) showed that decreasing $p(CO)$ from 0.67 to 0.13 atm resulted in a total polarization resistance increase from 1.1 to 1.7 Ω $cm^2$. These values were generally higher than those for comparable $H_2$–$H_2O$–Ar mixtures. The cathode contribution to the EIS spectra, which was especially small relative to the anode contributions in this fuel, was neglected. A model with two electrode processes represented by two Cole elements and centered at ~20 Hz and ~0.8 Hz, similar to the $H_2$–$H_2O$ model, was found to provide excellent fits to the data as shown in Fig. 6. For CO-rich mixtures, the lower frequency process

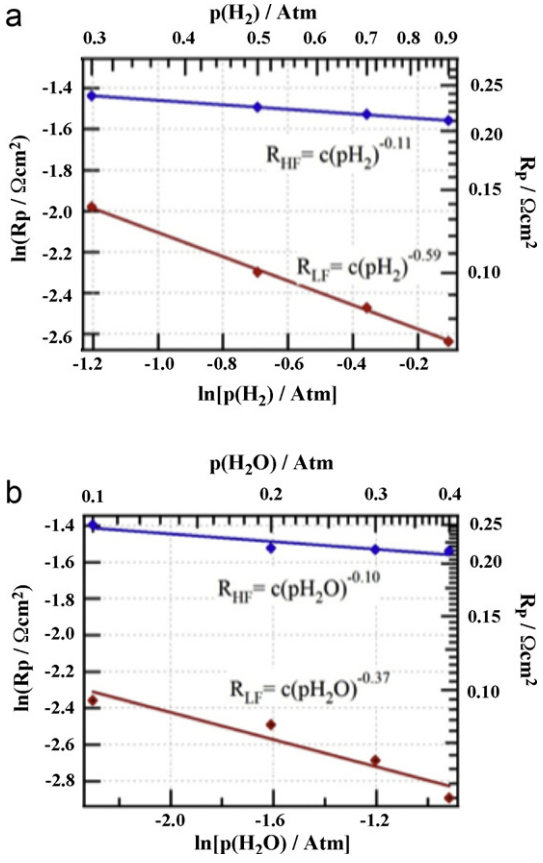


**Fig. 3.** Resistances $R_{HF}$ and $R_{LF}$, obtained from best fits to the data in Figs. 1 and 2, plotted versus $H_2$ (a) and $H_2O$ (b) partial pressure.

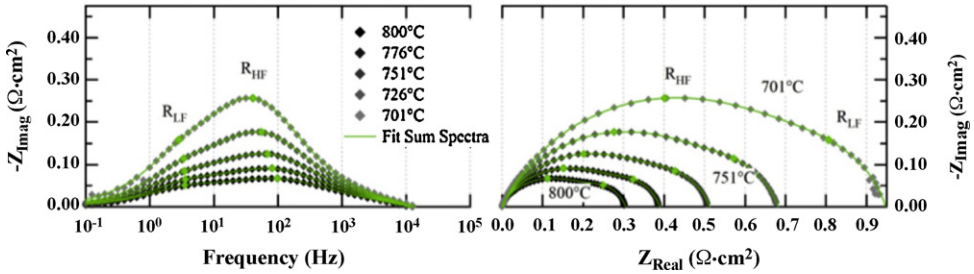


**Fig. 4.** Bode (left) and Nyquist (right) plots of the EIS data measured at 75%$H_2$ and 25% $H_2O$ at temperatures varied from 700 to 800 °C. The grey symbols indicate the measured data, green lines show the fit, and green symbols show the fitted element's characteristic frequencies. The ohmic contribution was subtracted from the cell resistance. (For interpretation of the references to color in this figure caption, the reader is referred to the web version of the article.)

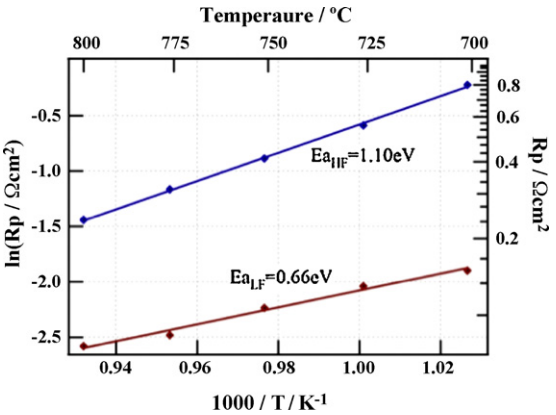


**Fig. 5.** Resistances $R_{HF}$ and $R_{LF}$, obtained from best fits to the data in Fig. 4, plotted versus inverse temperature.

dominates, although the higher frequency one is still detectable. For low CO content, the higher frequency response was too small for an unambiguous fit. Fig. 7 shows the effect of $p(CO_2)$, with the Ar content adjusted to maintain $p$(CO) constant. There was relatively little change in the total resistance with $p(CO_2)$.

Fig. 8 shows log–log plots of the resistances $R_{HF}$ and $R_{LF}$ versus $p$(CO) (a) and $p(CO_2)$ (b). The impedances increased with decreasing $p$(CO), qualitatively similar to the $H_2$ dependence shown above, but the HF impedance decreased with decreasing $p(CO_2)$, opposite to the trend observed for $p(H_2O)$. The values were fit reasonably well by power law dependences with $R_{HF} \propto p(CO)^{-0.29}$, $R_{LF} \propto p(CO)^{-0.25}$, $R_{HF} \propto p(CO_2)^{0.22}$, and $R_{LF} \propto p(CO_2)^{-0.11}$. Because of the opposing effects of $p(CO_2)$ on $R_{HF}$ and $R_{LF}$, the total anode polarization resistance changed only slightly with $CO_2$ partial pressure.

The temperature dependence of the EIS response was measured between 700 and 800 °C in a fuel containing 50% CO and 50%$CO_2$. The data along with fits, using the same circuit model as above, are shown in Fig. 9. Both $R_{HF}$ and $R_{LF}$ increased with decreasing temperature, with activation energies $E_{HF}$ = 0.78 eV and $E_{LF}$ = 1.29 eV, as shown in the Arrhenius plot of the resistances in Fig. 10. The frequency of $R_{HF}$ increased from 15 to 20 Hz and $R_{LF}$ increased from 0.3 Hz to 0.8 Hz from 700 to 800 °C. The ohmic resistance (not displayed) was thermally activated with $E_s$ = 0.69 eV, comparable to the value noted above for $H_2/H_2O$ operation.

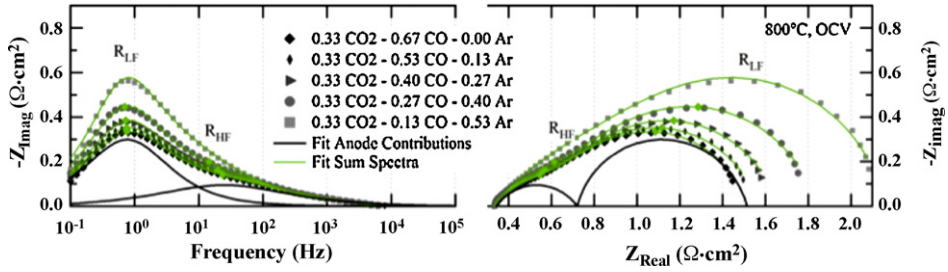


**Fig. 6.** Bode (left) and Nyquist (right) plots of the EIS data measured at 800 °C at open circuit with different CO partial pressures and fixed $CO_2$ partial pressure. The grey symbols indicate the measured data, green lines show the fits, black lines illustrate the individual fitted contributions for the high p(CO) case, and green symbols show the fit characteristic frequencies. (For interpretation of the references to color in this figure caption, the reader is referred to the web version of the article.)

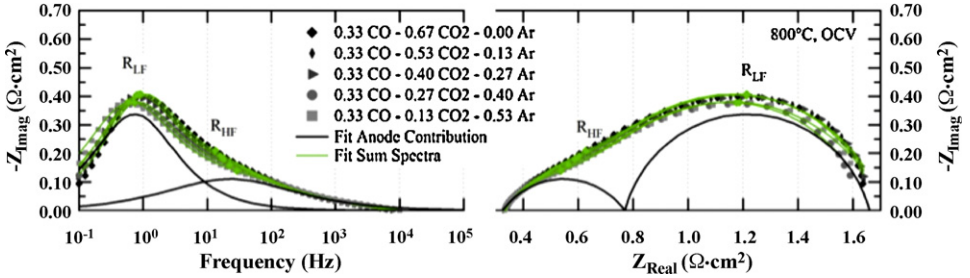


**Fig. 7.** Bode (left) and Nyquist (right) plots of the EIS data measured at 800 °C at open circuit with different $CO_2$ partial pressures and fixed CO partial pressure. The grey symbols indicate the measured data, green lines show the fits, black lines illustrate the individual fitted contributions for the $p(CO_2)$ = 0.27 atm case, and green symbols show the fit characteristic frequencies. (For interpretation of the references to color in this figure caption, the reader is referred to the web version of the article.)

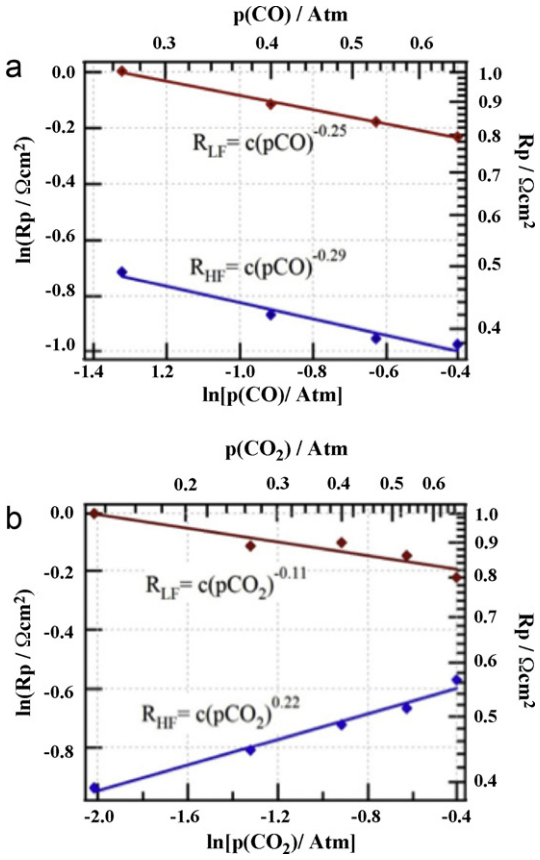


**Fig. 8.** Resistances $R_{HF}$ and $R_{LF}$, obtained from best fits to the data in Figs. 6 and 7, plotted versus CO (a) and $CO_2$ (b) partial pressure.

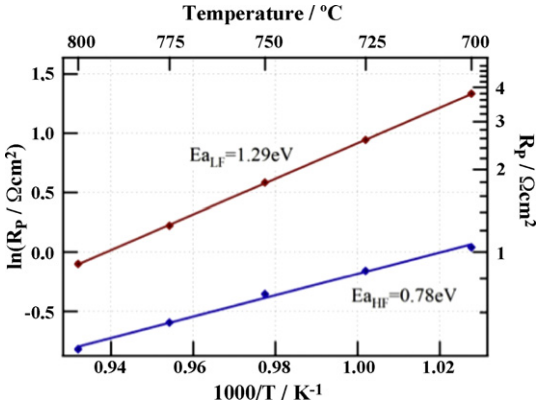


**Fig. 10.** Resistances $R_{HF}$ and $R_{LF}$ in 50%CO–50% $CO_2$, obtained from best fits to the data in Fig. 9, plotted versus inverse temperature.

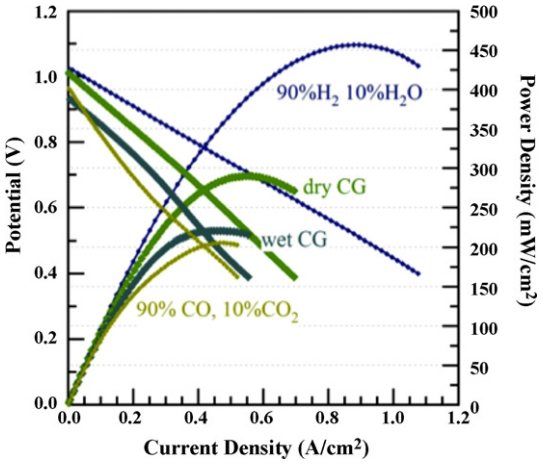


**Fig. 11.** Potential and power density versus current density for a cell operated on 90%$H_2$–10%$H_2O$, 90%CO–10%$CO_2$, wet coal gas (wet CG), and dry coal gas (dry CG).

### 3.3. $H_2$–$H_2O$–CO–$CO_2$ fuel

The LSCrRu–GDC cell was also tested in a surrogate coal syngas containing 28%$H_2O$, 28.7%$H_2$, 11.9%$CO_2$, 29.3%CO and 2.1%$N_2$, similar to the syngas composition reported in other studies [29,30]. A dry version of this fuel (39.9%$H_2$, 16.5%$CO_2$, 40.6%CO, 3%$N_2$) was also tested. The current–voltage characteristics in wet and dry coal syngas at 800 °C are shown in Fig. 11. The dry syngas shows a higher OCV and higher power density due to the higher concentrations of $H_2$ and CO. For comparison, the results for operation on 90%$H_2$–10%$H_2O$ and 90%CO–10%$CO_2$ are also shown. The power densities in wet coal gas (185 mW cm$^{-2}$ at 0.7 V) and dry coal gas (255 mW cm$^{-2}$ at 0.7 V) are much smaller than for 90%$H_2$–10%$H_2O$ (395 mW cm$^{-2}$ at 0.7 V), due in part to the lower open circuit voltage but also a result of a higher anode polarization resistance. These results illustrate that SOFCs operated on coal syngas will generally yield lower voltage and power density than for hydrogen fuel. The syngas power densities appear, at least approximately, to be averages of the power densities for $H_2$–$H_2O$ and CO–$CO_2$.

EIS results for wet syngas fuel versus temperature are displayed in Fig. 12. Processes for $R_{HF}$ (20–57 Hz) and $R_{LF}$ (1–3.5 Hz) were both thermally activated (Fig. 13) with $E_{HF}$ = 1.07 eV and $E_{LF}$ = 1.22 eV. As observed for operation in CO–$CO_2$, the characteristic frequency for both $R_{HF}$ and $R_{LF}$ decreased with decreasing temperature. The polarization resistance values for syngas tended to fall between those for $H_2$–$H_2O$ and CO–$CO_2$. For example, at

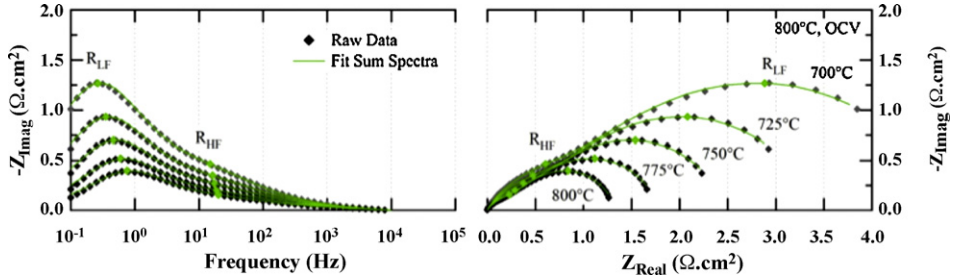


**Fig. 9.** Bode (left) and Nyquist (right) plots of the EIS data measured in 50%CO–50% $CO_2$ at temperatures varied from 650 to 800 °C. The grey symbols indicate the measured data, green lines show the fits, and green symbols show the fit characteristic frequencies. The ohmic contribution was subtracted from the cell resistance. (For interpretation of the references to color in this figure caption, the reader is referred to the web version of the article.)

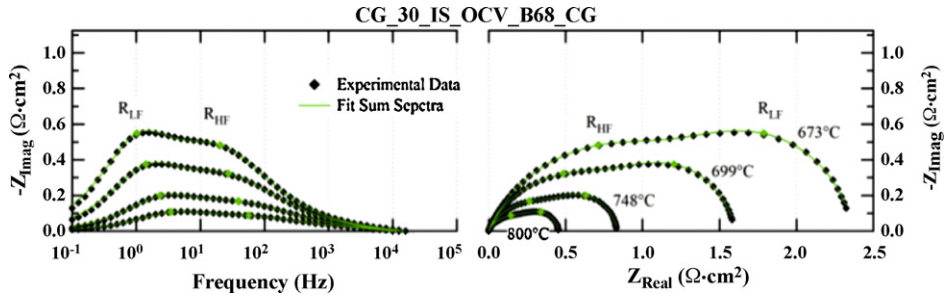


**Fig. 12.** Effect of temperature on cell impedance for an LSCrRu–GDC cell operating on wet coal syngas. The black symbols indicate the measured data, green lines show the fits, and green symbols show the fit characteristic frequencies. The ohmic contribution was subtracted from the cell resistance. (For interpretation of the references to color in this figure caption, the reader is referred to the web version of the article.)

800 °C, $R_P = 0.45\,\Omega\,cm^2$ for coal gas compared to $0.27\,\Omega\,cm^2$ for $H_2/H_2O$ and $1.3\,\Omega\,cm^2$ for $CO/CO_2$.

In order to further explore the role of CO and $CO_2$ during syngas-fueled operation, the syngas mixture results were compared with those from $H_2$–$H_2O$–Ar mixtures, i.e., replacing CO and $CO_2$ with inert Ar. The as-supplied syngas mixture noted above is not at equilibrium for the cell operating conditions ($P = 1$ atm and $T = 800$ °C), such that the fuel may undergo water-gas shift towards equilibrium. Because of the uncertainty in the extent of the water gas shift reaction at the anode, two different $H_2$–$H_2O$–Ar mixtures were employed to match the range of possible syngas constitutions. Table 2 gives the as-supplied and equilibrated syngas compositions, the latter calculated using Thermocalc, and the two $H_2$–$H_2O$–Ar mixture compositions. The equilibrated coal gas contains a higher concentration of $H_2$ and lower $H_2O$ than the as-supplied fuel. Fig. 14 shows the results, which are also summarized in Table 2: both $R_{HF}$ and $R_{LF}$ are clearly higher for syngas than for either $H_2$–$H_2O$–Ar mixture. That is, CO and/or $CO_2$ interfere with $H_2$ oxidation.

## 4. Discussion

### 4.1. Effect of fuel composition on anode processes

For all conditions tested here, the EIS data was fit well using a model with three Cole elements in series, although in some cases one of the elements, corresponding to the cathode contribution, was small enough to be omitted. Prior work on $La_{0.83}Sr_{0.19}CrO_3$ microelectrodes on YSZ electrolytes in $H_2$–$H_2O$ also showed two processes, with frequencies close to those shown in Figs. 1 and 2 [6]. This is also similar to reports for Ni-YSZ, where two coupled Cole elements were used to model the response, along with a separate element representing gas diffusion [4,31,32]. A mechanistic interpretation of the Ni-YSZ response has been made using a transmission-line model combining charge transfer elements representing three phase boundary (TPB) processes and elements associated with oxygen ion transport in the anode YSZ phase [3,32]. A similar explanation may also apply to the present anodes, with the two Cole elements representing a combination of ionic resistance in the GDC phase and a charge-transfer process at chromite-GDC and/or Ru-GDC TPBs. Even if the dominant process is at chromite-GDC TPBs, the dramatic resistance reduction associated with the Ru nano-particles suggests that Ru enhances a rate-limiting step in the hydrogen oxidation process [13]. These proposed mechanisms are thermally activated, consistent with the observed temperature dependences of the HF and LF resistances.

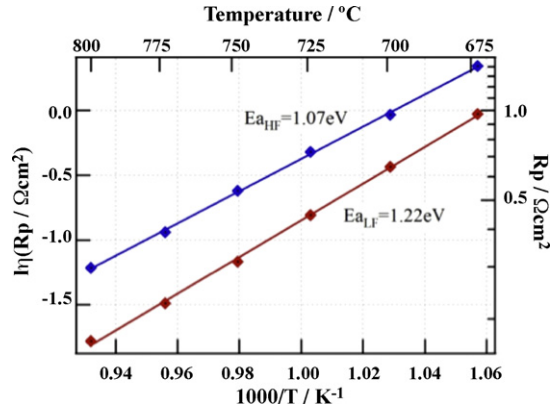


**Fig. 13.** Arrhenius plots of $R_{HF}$ and $R_{LF}$ for a cell operating on coal gas.

Switching the fuel from $H_2$–$H_2O$ to CO–$CO_2$ resulted in a polarization resistance increase by a factor of ~3–4. This general trend agrees with that observed for Ni-YSZ, where the charge transfer resistance increased by a factor of ~2 [32] in one case and ~10 [5] in another on switching from $H_2$ to CO. In the present case, the resistance increase is primarily due to a factor of ~10 increase in $R_{LF}$, which is the smaller resistance in $H_2$ but becomes the dominant resistance in CO because $R_{HF}$ increases by only a factor of ~2. Prior results on $La_{0.83}Sr_{0.19}CrO_3$ microelectrodes were generally similar, with $R_{HF}$ dominant in $H_2$–$H_2O$ and $R_{LF}$ dominant in CO–$CO_2$.

Table 3 summarizes the present activation energy results. The activation energies of $R_{LF}$ vary with fuel as $E_{a,\,H_2} < E_{a,\,coal\,gas} < E_{a,\,CO}$. The activation energies for $R_{HF}$ followed the opposite trend, with $E_{a,\,H_2} > E_{a,\,coal\,gas} > E_{a,\,CO}$. These results suggest a change in the oxidation reaction rate limiting steps with fuel type, with the CO oxidation reactions generally being slower with larger activation energies. Table 3 also shows literature data for both $La_{0.83}Sr_{0.19}CrO_3$ and Ni-YSZ anodes. Note that the values for Ni-YSZ are given for un-separated coupled Cole elements. For the chromite, activation energies for both resistance components were larger for CO–$CO_2$ versus $H_2$–$H_2O$ [6]. The activation energy for Ni-YSZ was also larger for CO–$CO_2$ compared to $H_2$–$H_2O$ [32].

Table 3 summarizes the power law values obtained from the observed dependences of the LF and HF resistances on the fuel partial pressures. The observation that the power values are different for CO–$CO_2$ versus $H_2$–$H_2O$ provides further evidence that the rate-limiting oxidation steps are different. Table 3 also shows the literature values of measured powers for $La_{0.83}Sr_{0.19}CrO_3$ and Ni-YSZ anodes, for comparison. The values for the present anodes and the $La_{0.83}Sr_{0.19}CrO_3$ anodes are similar except for the HF response in CO. One unusual feature of the present data is the positive exponent observed for the $p(CO_2)$ dependence. Positive exponents have also been observed in some cases for Ni-YSZ anodes [3]. This may indicate competitive adsorption between $CO_2$ and another species that limits fuel oxidation.

A striking contrast between the chromite results and those from Ni-YSZ is the difference in relaxation times. For Ni-YSZ, the

**Table 2**
Summary of coal gas and $H_2$–$H_2O$–Ar compositions used in the tests, along with the composition expected if the coal gas equilibrates. Also shown are measured and predicted OCV values. Note that the fuel nitrogen content (2.1%) is not shown.

| | Coal gas (as supplied) | Coal gas (equilibrated) | Test #1 | Test #2 |
|---|---|---|---|---|
| $p(H_2O)$ (atm) | 0.280 | 0.224 | 0.28 | 0.23 |
| $p(H_2)$ (atm) | 0.287 | 0.338 | 0.29 | 0.35 |
| $p(CO_2)$ (atm) | 0.119 | 0.172 | – | – |
| $p(CO)$ (atm) | 0.293 | 0.237 | – | – |
| $p(Ar)$ (atm) | – | – | 0.44 | 0.42 |
| OCV (measured) (V) | 0.937 | | 0.935 | 0.951 |
| OCV (theoretical) (V) | | 0.961 | 0.941 | 0.959 |
| $R_{HF}$ ($\Omega\,cm^2$) | 0.27 | | 0.23 | 0.22 |
| $R_{LF}$ ($\Omega\,cm^2$) | 0.26 | | 0.17 | 0.14 |

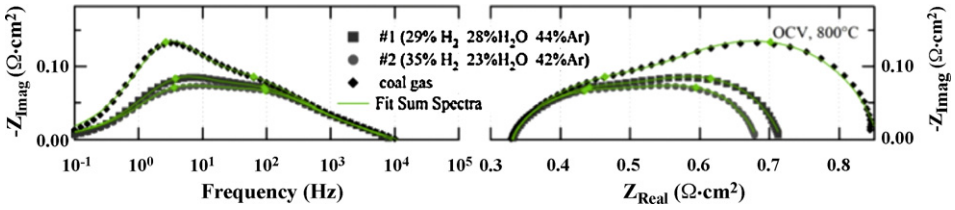


**Fig. 14.** Impedance spectra recorded from an LSCrRu–GDC (left) cell operated in coal gas; 29%$H_2$, 28%$H_2O$, and 44%Ar; and 35%$H_2$, 23%$H_2O$, and 42%Ar. The grey symbols indicate the measured data, green lines show the fits, and green symbols show the fit characteristic frequencies. (For interpretation of the references to color in this figure caption, the reader is referred to the web version of the article.)

characteristic frequencies of the arcs due to activation polarization were 200–3000 Hz for the low frequency arc and 3–50 kHz for the high frequency arc [31,32]. These values are 100–1000 times higher than for the chromite anodes, where $R_{LF}$ varied between 0.1–10 Hz and $R_{HF}$ varied between 10–100 Hz. The characteristic frequency of a Cole element is given by the expression:

$$f_c\,(\mathrm{Hz}) = \frac{1}{2\pi Q R^{(1/n)}} \quad (1)$$

where $R$ is the process effective resistance and $Q$ is the effective capacitance. The present anode resistances were ~10 times those for Ni-YSZ anodes [31,32], suggesting that there was also a substantially larger capacitance. This may be a "chemical capacitance" associated with oxygen content changes that can occur in perovskites as a function of applied potential [33].

### 4.2. Performance in coal gas

Syngas fuel yielded substantially higher resistance than similar $H_2$–$H_2O$–Ar fuel mixtures. That is, replacing CO and $CO_2$ with inert Ar actually improved cell performance. One possible explanation is that CO and/or $CO_2$ adsorb too strongly on important surface sites, resulting in reduced $H_2$ and/or $H_2O$ coverages or low vacant site densities, negatively impacting the fuel oxidation process. This may relate to the positive power law dependence of $R_p$ on $p(CO_2)$ (Fig. 8b), which suggests that $CO_2$ may adsorb preferentially onto surface sites required for fuel oxidation. For example, a positive exponent was explained, for the case of a Pt cathode on doped $CeO_2$, by too-high oxygen coverages leading to low availability of vacant sites [34].

This syngas behavior for LSCrRu–GDC is significantly different than what has been observed in Ni-YSZ anode supported cells. For Ni-YSZ cells, the polarization resistance is essentially unaffected by additions of CO and $CO_2$ [5]. This phenomena is likely due to the water-gas shift reaction, enabled by the thick

**Table 3**
Comparison of anode characteristics.

| | LSCrRu–GDC | | LSCr Ref. [4] | | Ni-YSZ Refs. [1,29,30] |
|---|---|---|---|---|---|
| | LF | HF | LF | HF | Anode charge transfer resistance |
| $H_2$–$H_2O$ | | | | | |
| $E_a$ (eV) | 0.66 | 1.10 | 1.12 | 1.32 | 1.09[a] |
| $p(H_2)^x$ | −0.59 | −0.11 | −0.5[b] | ~0 | 0.10[c] |
| $p(H_2O)^x$ | −0.37 | −0.10 | – | – | −0.33[d] |
| CO–$CO_2$ | | | | | |
| $E_a$ (eV) | 1.29 | 0.78 | 1.98 | 1.6 | 1.23 |
| $p(CO)^x$ | −0.25 | −0.29 | −0.25[e] | ~0 | 0.058[f] |
| $p(CO_2)^x$ | −0.11 | 0.22 | – | – | −0.25[g] |
| Coal gas (wet) | | | | | |
| $E_a$ | 1.22 | 1.07 | – | – | – |

[a] Ref. [29] $p(H_2) = 0.8$ atm, $p(H_2O) = 0.2$ atm.
[b] Ref. [4] $T = 850\,^\circ$C, $p(H_2O) = 0.072$ atm.
[c] Ref. [29] $T = 800\,^\circ$C, $p(H_2O) = 0.2$ atm.
[d] Ref. [29] $T = 800\,^\circ$C, $p(H_2) = 0.6$ atm.
[e] Ref. [4] $T = 850\,^\circ$C, $p(CO_2) = 0.02$ atm.
[f] Ref. [1] $T = 800\,^\circ$C, $p(CO_2) = 0.2$ atm.
[g] Ref. [1] $T = 800\,^\circ$C, $p(CO) = 0.4$ atm.

catalytically active support. Indeed, when Ni-YSZ anode supported cells were directly compared to thin-film Ni-YSZ anodes in mixtures of $CO/H_2/CO_2/H_2O$, the thin film anode performance was strongly affected by the gas constitution [5]. The authors attributed the striking change in anode behavior to a loss in activity for the water-gas shift reaction due to less Ni in the anode [5]. The present LSCrRu–GDC anodes are presumably similar to the thin-film Ni-YSZ in this regard: the volume of Ru catalyst is too small to provide significant water gas shift activity [35].

## 5. Conclusions

The effect of syngas fuel composition on the performance of the LSCrRu–GDC anode was studied. The anode polarization resistance was dominated by two impedance processes that followed power-law variations with fuel component partial pressures. Furthermore, these processes were thermally activated, indicating that the two anode arcs were related to activation polarization. The polarization resistance in coal gas was higher than expected based on the $H_2$ and $H_2O$ contents alone, indicating that the CO and/or $CO_2$ present in syngas interfered with $H_2$ oxidation.

## Acknowledgments

The authors gratefully acknowledge support from the National Science Foundation (Grant # CBET-0854223), the Department of Energy (Grant # DE-FG02-05ER46255), and the California Energy Commission's Energy Innovations Small Grant Program (Grant #: 55178A/07-02).

## References

[1] K. Yamaji, H. Kishimoto, Y.P. Xiong, T. Horita, N. Sakai, M.E. Brito, H. Yokokawa, Journal of Power Sources 159 (2006) 885–890.
[2] Y.B. Lin, Z.L. Zhan, J. Liu, S.A. Barnett, Solid State Ionics 176 (2005) 1827–1835.
[3] A. Leonide, S. Hansmann, A. Weber, E. Ivers-Tiffée, Journal of Power Sources 196 (2011) 7343–7346.
[4] A. Leonide, V. Sonn, A. Weber, E. Ivers-Tiffee, Journal of the Electrochemical Society 155 (2008) B36–B41.
[5] Y. Jiang, A.V. Virkar, Journal of the Electrochemical Society 150 (2003) A942–A951.
[6] P. Vernoux, Ionics 3 (1997) 270–276.
[7] R.J. Kee, H.Y. Zhu, A.M. Sukeshini, G.S. Jackson, Combustion Science and Technology 180 (2008) 1207–1244.
[8] H. Uchida, N. Mochizuki, M. Watanabe, Journal of the Electrochemical Society 143 (1996) 1700–1704.
[9] B.D. Madsen, W. Kobsiriphat, Y. Wang, L.D. Marks, S.A. Barnett, Journal of Power Sources 166 (2007) 64–67.
[10] W. Kobsiriphat, B.D. Madsen, Y. Wang, M. Shah, L.D. Marks, S.A. Barnett, Journal of the Electrochemical Society 157 (2010) B279–B284.
[11] D.M. Bierschenk, E. Potter-Nelson, C. Hoel, Y. Liao, L. Marks, K.R. Poeppelmeier, S.A. Barnett, Journal of Power Sources 196 (2011) 3089–3094.
[12] Y. Wang, B.D. Madsen, W. Kobsiriphat, S.A. Barnett, L.D. Marks, Microscopy and Microanalysis 13 (2007) 100–101.
[13] W. Kobsiriphat, B.D. Madsen, Y. Wang, L.D. Marks, S.A. Barnett, Solid State Ionics 180 (2009) 257–264.
[14] A. Atkinson, S. Barnett, R.J. Gorte, J.T.S. Irvine, A.J. McEvoy, M. Mogensen, S.C. Singhal, J. Vohs, Nature Materials 3 (2004) 17–27.
[15] C.W. Sun, U. Stimming, Journal of Power Sources 171 (2007) 247–260.
[16] J.B. Goodenough, Y.-H. Huang, Journal of Power Sources 173 (2007) 1–10.
[17] J.M. Haag, B.D. Madsen, S.A. Barnett, K.R. Poeppelmeier, Electrochemical and Solid-State Letters 11 (2008) B51–B53.
[18] Z. Cheng, M. Liu, Solid State Ionics 178 (2007) 925–935.
[19] Y. Matsuzaki, I. Yasuda, Solid State Ionics 132 (2000) 261–269.
[20] J.N. Kuhn, N. Lakshminarayanan, U.S. Ozkan, Journal of Molecular Catalysis A: Chemical 282 (2008) 9–21.
[21] C.M. Finnerty, N.J. Coe, R.H. Cunningham, R.M. Ormerod, Catalysis Today 46 (1998) 137–145.
[22] K. Sasaki, Y. Teraoka, Journal of the Electrochemical Society 150 (2003) A878–A884.
[23] Y.B. Lin, Z.L. Zhan, S.A. Barnett, Journal of Power Sources 158 (2006) 1313–1316.
[24] D. Waldbillig, A. Wood, D.G. Ivey, Solid State Ionics 176 (2005) 847–859.
[25] S.W. Tao, J.T.S. Irvine, Nature Materials 2 (2003) 320–323.
[26] D.M. Bierschenk, J.M. Haag, K.R. Poeppelmeier, S.A. Barnett, in: M.D.S.C. Singhal (Ed.), Solid Oxide Fuel Cells 11 (SOFC-XI), Electrochemical Society, Vienna, Austria, 2009, pp. 2107–2116.
[27] T. Ishihara, H. Matsuda, Y. Takita, Journal of the American Chemical Society 116 (1994) 3801–3803.
[28] D.M. Bierschenk, M.R. Pillai, Y. Lin, S.A. Barnett, Fuel Cells 10 (2010) 1129–1134.
[29] R.S. Gemmen, J. Trembly, Journal of Power Sources 161 (2006) 1084–1095.
[30] J.P. Trembly, R.S. Gemmen, D.J. Bayless, Journal of Power Sources 171 (2007) 818–825.
[31] V. Sonn, A. Leonide, E. Ivers-Tiffee, Journal of the Electrochemical Society 155 (2008) B675–B679.
[32] A. Leonide, Institut für Werkstoffe der Elektrotechnik, Karlsruhe Institute of Technology, Karlsruhe, Germany, 2010.
[33] S.B. Adler, Chemical Reviews 104 (2004) 4791–4843.
[34] D.Y. Wang, A.S. Nowick, Journal of the Electrochemical Society 126 (1979) 1155–1165.
[35] P. Vernoux, E. Djurado, M. Guillodo, Journal of the American Ceramic Society 84 (2001) 2289–2295.